J Ther Eng, Vol. 10, No. 4, pp. 961−977, July, 2024

Journal of Thermal Engineering
Web page info: https://jten.yildiz.edu.tr
DOI: 10.14744/thermal.0000849

Journal of Thermal Engineering

Research Article

Comparative analysis of modified jet diffuser geometry for evaluating the impact of rounded edges and chamfered design on cooling efficiency of electronic components in cross flow and impinging jet

Abdelhak FELLAGUE CHEBRA[1], Ali KHELIL[1,*], Mohamed BRAIKIA[1], Mohammed BEDROUNI[1]

[1]*Laboratory of Control, Testing, Measurement and Mechanical Simulation, University of Chlef, Chlef, B. P. 151, 2000, Algeria*

ARTICLE INFO

Article history
Received: 21 June 2023
Revised: 10 September 2023
Accepted: 11 September 2023

Keywords:
Cooling Electronic Components; Impinging Jet; Lobed Jet; Jet Cross Flow; Wall-Mounted Cube

ABSTRACT

This article investigates the influence of altering the geometry of a jet diffuser and modifying the top corners of electronic components on cooling effectiveness. Computational simulations using the Shear stress transport turbulence model (*k-ω SST)* are conducted. The study considers a cross-flow Reynolds number of 3410 and varying impinging jet Reynolds numbers ($\alpha = Re_j/Re_H = 0.5$, 1, and 1.5). Results show a clear relationship between flow structure and cooling effectiveness. At $\alpha = 0.5$, cubes with rounded edges and chamfered corners have lower cooling efficiency. At $\alpha = 1.0$, chamfered cubes demonstrate enhanced cooling efficiency (4.7% increase in average Nusselt number). At $\alpha = 1.5$, rounded cubes exhibit superior cooling performance (3.7% higher Nusselt number). A lobed diffuser configuration achieves outstanding cooling effectiveness, with a Nusselt number 15% higher than a circular jet. These findings provide insights for improving cooling efficiency in electronic components under cross-flow and impinging jet conditions.

Cite this article as: Fellague Chebra A, Khelil A, Braikia M, Bedrouni M. Comparative analysis of modified jet diffuser geometry for evaluating the impact of rounded edges and chamfered design on cooling efficiency of electronic components in cross flow and impinging jet. J Ther Eng 2024;10(4):961−977.

INTRODUCTION

The utilization of jets is extensive, encompassing a broad spectrum of applications such as ventilation, cooling, shaping of glass, drying of textiles and paper materials, cooling of turbines and electronics, and the vital function of de-icing airplane wings and engine inlets [1-5]. The domain of electronics is beset by a formidable challenge owing to the imperious need for stringent thermal regulation of microprocessor chips and other integral constituents to ensure their continued durability and dependable performance over a protracted duration [6]. There is a plethora of cooling techniques available for electronic components, encompassing the pin-fin heat sink, confined jet impingement, geothermal energy and heat pipes. The implementation of various cooling methods, such as air flows, dielectric liquid-cooled systems, Nano fluids (water-aluminum oxide

***Corresponding author.**
*E-mail address: a.khelil@univ-chlef.dz

This paper was recommended for publication in revised form by Editor-in-Chief Ahmet Selim Dalkılıç

Published by Yıldız Technical University Press, İstanbul, Turkey

and water-titanium dioxide and alumina-Cu-water), thermoelectric effects, and liquid immersion systems, among others, has enabled an improvement in thermal performance for electronic equipment, as stated in references [7-13]. However, it is important to highlight that the present study specifically centres on cooling electronic components using air as the working fluid. As indicated in the existing literature, contemporary research has evidenced that substitute fluids (Nano fluid) exhibit thermal characteristics that exceed those of air as shown in the study of Jalili et al. [14] this study's objective is the examination of convective heat transfer within a turbulent flow double-tube heat exchanger, aimed at optimizing fluid heating and cooling processes. The fluids utilized encompass Nano fluids, a composition of water and aluminium oxide, along with a mixture of water and titanium dioxide. Notably, the findings highlight the superior heat transfer performance of Nano fluids, exhibiting a substantial 12% improvement at a concentration of 6%. Furthermore, efficiency gains of 81% and 85% are evident for rectangular and curved fins, respectively. To attain a thorough understanding of intricate material categorizations and their profound implications on thermal performance, coupled with a meticulous elucidation of experimental thermal analysis, I recommend consulting the following references [15-17]. However, this fact does not reduce the significance of air as a highly utilized fluid within the electronics sector. Although its thermal capabilities have certain shortcomings, the simplicity of its implementation, low system complexity, and potential for optimizing the cooling process render air a highly attractive option. These have primarily centred on the optimization and regulation of cooling processes to ensure the safe operation of said devices within designated temperature ranges. An illustration of utilizing air as a cooling fluid for electronic components is exemplified in the study undertaken by Castro and Robins [18]. In their experimental study, the scientists used a hotwire anemometer as the main instrument for measuring the velocity field around a cube mounted on a flat plate. The researchers observed that the dimensions of both the recirculation zone located in the wake region behind the cube and the vortex surrounding the cube are influenced by the specific

flow conditions and the respective boundaries at the inlet. Hearst et al. [19] conducted an experimental inquiry in order to analyse the impact of turbulence on the wake of a cube mounted on a vertical wall. The researchers accomplished this objective through the development of turbulent boundary layers featuring diverse degrees of turbulence intensity, while simultaneously preserving comparable shear profiles. The scholars utilized the methods of particle image velocimetry and hot-wire anemometry to conduct experimentation. The experiments were performed with a Reynolds number of 1800000 and a ratio of cube elevation to boundary layer thickness of 0.47. The researchers' investigation indicated that the location at which reattachment occurs in the wake region, as well as the average stagnation point, exhibit no discernible alterations as a consequence of the incoming profile. Furthermore, it was observed that an increase in turbulence intensity while maintaining constant normalized shear results in a reduction of the wake length. Tummers et al. [20] elaborated an experimental investigation was carried out to examine the patterns of fluid flow and temperature dispersal on the surfaces of five successive cubes that were integrated into the lower wall of a channel, upon the application of a jet that was perpendicular to it. The results of the study unveiled the complex characteristics of the flow configuration, such as the formation of vortices, zones of backflow, deceleration zones, the influence of curvature, stagnation, and separation points. Each of the aforementioned phenomena had a notable impact on the thermal properties of the walls of the cubic structures. Nakamura et al. [21] conducted an empirical investigation on the fluid dynamics and localized heat transfer near a wall-mounted cube. The present study entailed the examination of five distinct Reynolds numbers, ranging from 4200 to 33000, in relation to the height of the cube and the inlet velocity. The scientists observed a direct relationship between the transfer of heat and the morphology of the flow. A horseshoe vortex was observed to form in front of and on both sides of the cube, indicating enhanced heat transfer. An empirical study was conducted by Y. Masip et al. [22] to analyze the turbulent flow surrounding a wall-mounted cube positioned at the center of a channel, exposed to the combined impacts of cross-flow and impinging jet. The investigation encompassed three distinct cross-flow Reynolds numbers (Re_H) and three ratios of impinging to cross-flow Reynolds numbers (Re_j/Re_H). To measure the instantaneous flow velocity on multiple planes, Planar Particle Image Velocimetry was employed, enabling the determination of mean velocity and Reynolds stresses. The researchers concluded that the impact of the Reynolds number ratio on the flow morphology surrounding the component outweighs that of the cross-flow Reynolds number (Re_H). The analysis of flow morphology included the examination of vortices, recirculation bubbles, detachment, and reattachment zones for all nine test cases. The objective of this experimental investigation was implemented by Attalla et al. [23] is to examine the average heat transfer resulting from the impingement of an air jet on a rough plate using a micro cubic pin. Specifically, the study was to examine the influence of varying surface roughness levels on both the local and average Nusselt number. The micro cubic pin is characterized by its dimensions of 400 μm in both length and width, and variable depths ranging from 100 μm to 300 μm. As a result, the degree of surface roughness spans between 1.0, which signifies a smooth surface, to 1.64, 2.28, and 2.92. The Reynolds number fluctuates between 3150 and 10150. The findings indicate that, compared to a smooth surface, the average Nusselt number for the rough plate demonstrates an improvement ranging from 9.9% to 32.17%. The extent of this enhancement relies on the roughness degree, as well as the Reynolds number

and separation distance. According to Saleha et al. [24] a computational investigation was performed to examine the impact of modifying the geometric configuration on the efficiency of cooling. Their research specifically concentrated on beveling the upper edges of the cuboid. The simulations were performed using the *k-ω* SST (Shear Stress Transport) model at a Reynolds number of 3410, based on the overall velocity and channel height. The researchers examined three different ratios, comparing the Reynolds number of the impinging flow to the transverse flow (Re_j/Re_H = 0.5, 1, and 1.5). Their findings indicated that modifying the geometries did not lead to significant cooling enhancement for Re_j/Re_H = 0.5 and 1. However, for Re_j/Re_H = 1.5, the authors reported a substantial 26% improvement in cooling efficiency when using a cube with a chamfer height of 4 mm, as compared to a standard cube.Bedrouni and Khelil [3] conducted a study to explore the impact of curved upper corners of electronic components on the efficiency of cooling when subjected to cross-flow and perpendicular impinging jet. Simulations were conducted using the Shear stress transport *k-ω* model and the Reynolds Averaged Navier Stokes (RANS) equations to examine the impact of Reynolds number ratio on heat transfer in various cube geometries. The results revealed that increasing the Reynolds number ratio from impinging to cross-flow led to enhanced heat transfer for all cube configurations. Additionally, introducing curved upper corners to the cube resulted in a notable improvement in cooling efficiency, with enhancements exceeding 6% and 23% for α = 1 and 1.5, respectively, compared to a standard cube. Boudraa and Bessaïh [25] piloted a numerical investigation encompassing the intricate dynamics of turbulent three-dimensional forced convection flow, surrounding a thermally stimulated cubic obstruction, subject to a transverse flow and a colliding jet. The primary objective of the study was to assess the impact of the Reynolds number ratio on flow dynamics and heat transfer, utilizing the conventional *k-e* turbulence model. Additionally, the investigation aimed to examine the effects of channel height and jet axis positioning. The findings evince a noteworthy correlation between an increase in the Reynolds number ratio and a marked improvement in heat transfer. Furthermore, an increased velocity of the impinging jet was found to enhance cooling effectiveness in the uppermost region of the cubic block. Decreasing the channel height and shifting the jet axis towards the channel inlet exhibited a positive influence on heat transfer performance. Macia et al. [26] carried out an experimental investigation to study the effects of parametric variations on the cooling of electronic components, employing a combination of directed jet and conduit flow arrangement. The study examined three geometric parameters (*h/H*, *D/H*, *S/H*) and two fluid flow parameters (Re_H and U_j/U_m). The research findings demonstrate that Re_H, U_j/U_m, and *h/H* exert the most significant influence on heat transfer, resulting in an approximate 60% increase in the Nusselt number. Moreover, the findings of the study suggest that a reduction in the velocity ratio, at the point of the maximum jet diameter and jet-component eccentricity, in tandem with a decrease in the channel Reynolds number, results in heat transfer improvement with minimal losses in mechanical energy. Khan and Saha [27] studied the effect of jet impingement on turbulence and heat transfer in a heating cube arranged in a cross-flow arrangement. It was shown that, in the base case, heat transfer is poor on the top and sides of the cube, making them potential targets for jet impingement cooling. The researchers used finite volume techniques and a shear-enhanced Smagorinsky model to solve the Navier-Stokes and energy equations. Overall, this study provides insights into the turbulent structure and heat transfer properties affected by the jet impinging on the cube surface. Joshi et al. [28-31] investigated the slurry flow characteristics through 90° horizontal pipe bend. Eulerian multiphase model coupled with RNG *k-ε* turbulence model is used for a wide range of velocities V_m = 3–5 m/s and different Prandtl numbers. The transportation parameters like pressure distribution, concentration distribution, head loss, settling velocity, and specific energy consumption have benne determined. The authors concluded that the numerical predictions and procedures for the mixture of solid concentrations are generally in good agreement with the past experimental data available in the literature.

Drawing from the insights gleaned through the literature review, a conspicuous gap emerges in the realm of investigating the configuration of the impinging jet and its interaction with a cube face in relation to cooling efficiency. Consequently, the present study delves into an exploration of the impacts stemming from alterations in jet diffuser geometry and subtle adjustments to the upper cube face encompassing features like rounded edges and chamfered corners on the efficacy of electronic component cooling. In order to improve both cost-efficiency and aesthetic appeal in the design of air diffusion terminal units, a "passive" approach has been utilized to enhance air diffusion efficiency [32-34]. The present investigation focuses on employing a diffuser equipped with lobes to control the flow of a jet. The effectiveness of these geometric structures has been well-established in the fields of aeronautics and aerospace. As a result, they are now being integrated into the design of ejectors used in reactor exits. This study aims to utilize these lobed diffusers to enhance the thermal management of electronic components.

DESCRIPTION OF THE PROBLEM AND MATHEMATICAL EXPRESSIONS

Problem Formulation and Limiting Constraints

The current study focuses on the investigation of three electronic components, represented by cube-shaped structures. These components include a regular cube, a chamfered cube with a height of 2 mm, and a rounded cube with edges having a radius of 2 mm (Fig. 1). These cubes are

identified as 1, 2, and 3, respectively, in Figure 1, centrally located within a square channel, which is subjected to a transverse flow and a perpendicular impacting jet. The configuration employed bears a strong semblance to the experimental parameters expounded upon in Masip et al. [22]. To validate our computational findings with respect to the previously mentioned experiment, Figure 2 illustrates a diagrammatic representation of the geometric characteristics of the computational domain, along with the corresponding boundary conditions. The height of the component is denoted as h = 15 mm, while the total length of the channel along the x-axis is defined as 20h, where h represents the height of the cube. The breadth of the channel is characterized by a measurement of 15h, while the vertical scope of the domain extends to 2h along the y-axis. The cooling medium consists of incompressible air at a temperature of 293 K. The current investigation is conducted at a Reynolds number (Re_H) of 3410, determined

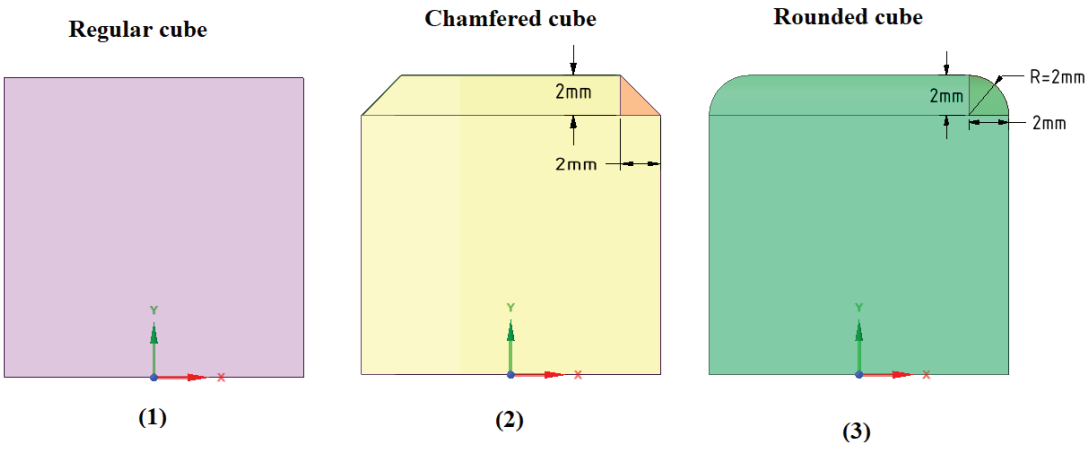

Figure 1. Different types of cube configurations.

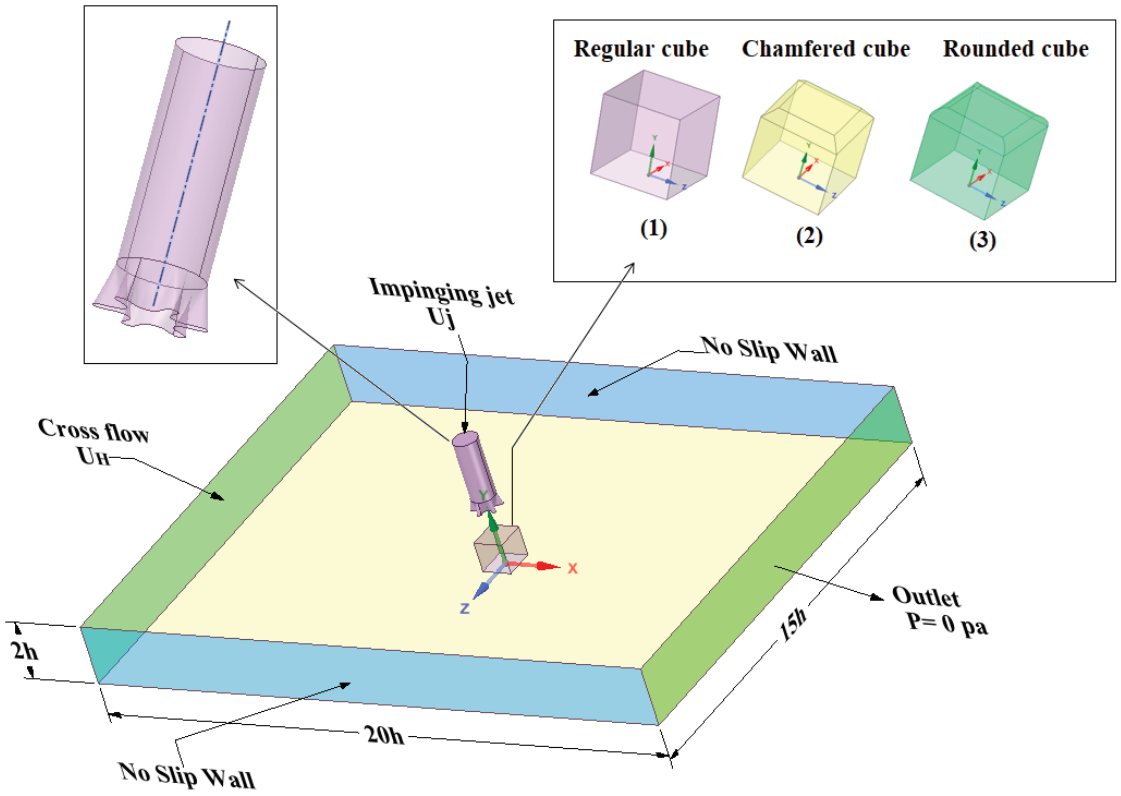

Figure 2. Diagram illustrating the computational domain incorporating the boundary conditions.

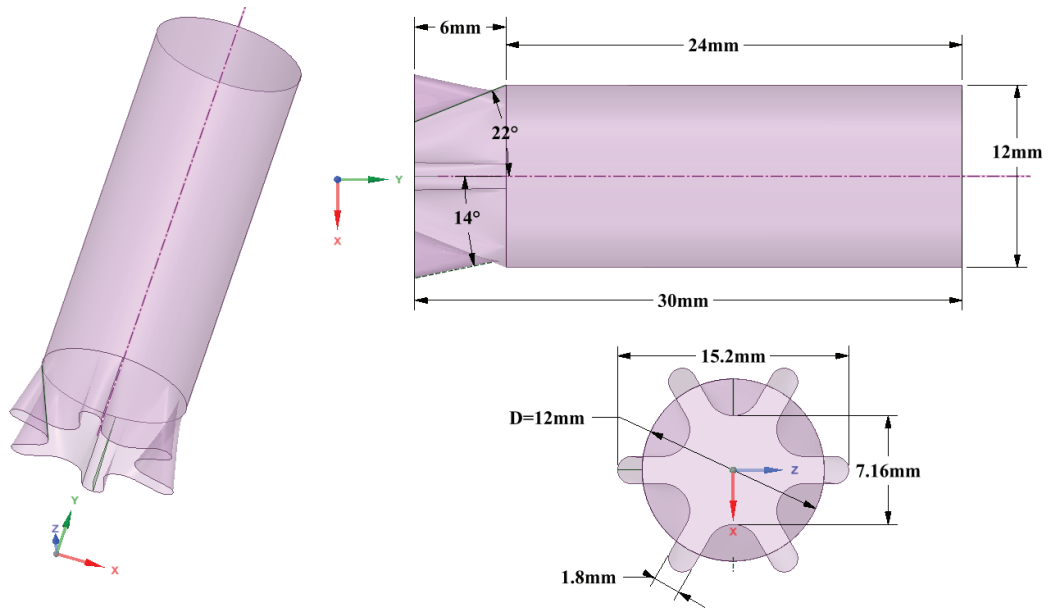

Figure 3. Lobed jet diffuser geometry.

by employing the cross-flow inlet velocity (U_H) and the channel height ($H = 2h$) for the cross-flow phenomenon. Alongside the flow within the channel, the component experiences a perpendicular impinging jet, which can adopt the form of a lobed jet. A study was undertaken to examine the effects of three different Reynolds number ratios on the interaction between the impinging jet and the channel flow. Inlet boundary conditions were defined for both the channel flow and the impinging jet, employing a temperature of 293 K. At the outlet, a relative pressure of $P = 0$ Pa was applied. The remaining boundaries were considered as smooth walls with no-slip conditions, maintaining a temperature equivalent to the fluid temperature of 293 K, except for the heated cube, which was assigned a temperature of 348 K. Further details can be found in Table 1.

Figure 3 illustrates the configuration of the lobed diffusers employed in this investigation. The nozzle comprises a circular conduit with a diameter $D = 12$ mm, featuring a floral design at the outlet. The outlet section showcases six inclined lobes with parallel edges and six undulating depressions. The angles of inner and outer penetration are denoted as θin = 22° and θout = 14°, correspondingly. Each lobe measures 6 mm in length and 1.8 mm in height.

Limiting Conditions

As previously mentioned, the geometric properties and computational variables bear a remarkable resemblance to those observed in the empirical investigation carried out by Masip et al. [22]. The limiting conditions of significance in the numerical simulation conducted in this study are compiled in Table 1.

Table 1. The parameters and limiting conditions used in the simulation settings

Variables	Conditions
Convergence criterion	10^{-6} for energy, 10^{-5} for the other variables
Turbulence intensity	5 %
Height of the cube	$H = 15$mm
Cross Flow Reynolds Number	$Re_H = 3410$
Air density	$\rho = 1.225$ Kg.m^{-1}
Nozzle diameter	$D = 12$mm
Inlet condition (cross flow)	$U = 1.705$ m s^{-1} and $T = 293$ K
Exit (pressure outlet)	$P = 0$Pa and $T = 293$K
All walls	No-slip wall: $U = 0$ m s^{-1} and $T = 293$ K
Wall (cube)	$T = 348$ K

Numerical Details

Turbulent flow characterization

The current study assumes that the fluid is incompressible and that the flow is in a statistically steady state. The continuity and momentum equations, also known as RANS equations, are expressed in differential form and can be represented using tensor notation, as described in references [2,3] and [35,36]

$$\frac{\partial U_i}{\partial x_i} = 0 \tag{1}$$

$$\rho \frac{\partial \left(U_i U_j\right)}{\partial x_j} = -\frac{\partial P}{\partial x_i} + \frac{\partial}{\partial x_j}\left[\mu\left(\frac{\partial U_i}{\partial x_j} + \frac{\partial U_j}{\partial x_i}\right) - \rho\overline{u_i' u_j'}\right] \tag{2}$$

$$\rho C_p U_i \frac{\partial T}{\partial x_i} = \frac{\partial}{\partial x_i}\left[\lambda \frac{\partial T}{\partial x_i} - \rho C_p \overline{u_i' T'}\right] \tag{3}$$

Mean velocity and temperature are represented by U_i and T, respectively, while other parameters include μ for dynamic viscosity, ρ for fluid density, P for pressure, C_p for specific heat capacity at constant pressure, λ for thermal conductivity, u_i', u_j' and T' for corresponding fluctuation components, $-\rho\overline{u_i' u_j'}$ and $-\rho C_p \overline{u_i' T'}$ for average Reynolds stresses and turbulent heat fluxes. To obtain a complete set of equations, models for $-\rho\overline{u_i' u_j'}$ and $-\rho C_p \overline{u_i' T'}$ are required to close the equations, as discussed in [37-41].

The channel walls and cube faces are assumed to adhere to a no-slip condition

$$U = 0_{|walls} \tag{4}$$

This work utilizes the *SST k-ω* model, which is founded on the Boussinesq eddy viscosity hypothesis, to derive the Reynolds stresses [42]

$$-\rho\overline{u_i' u_j'} = \mu_t\left(\frac{\partial U_i}{\partial x_j} + \frac{\partial U_j}{\partial x_i}\right) - \frac{2}{3}\left(\rho k + \mu_t \frac{\partial U_i}{\partial x_i}\right)\delta_{ij} \tag{5}$$

Here, turbulent viscosity is represented by μ_t turbulent kinetic energy by k, and strain rate tensor by δ_{ij}. Utilizing the Boussinesq approximation, which assumes that the heat flux is proportional to the turbulent eddy viscosity, the turbulent heat fluxes can be described using equations [43-45].

$$-\rho\overline{u_i' T'} = \frac{\mu_t}{\mathrm{Pr}_t}\frac{\partial T}{\partial x_i} \tag{6}$$

The turbulent Prandtl number, denoted by Pr_t, is a parameter used to evaluate turbulence mixing efficiency [45] and is set to $Pr_t = 0.85$ for this study. The *SST k-ω* turbulence model, developed by Menter [46], is widely used due to its accurate representation of flow physics and numerical stability. This model is a combination of the *k-ε* and standard *k-ω* models, and its formulation can be found in [47-48].

$$\frac{\partial \rho U_j k}{\partial x_j} = \frac{\partial}{\partial x_j}\left[\left(\mu + \sigma_k \mu_t\right)\frac{\partial k}{\partial x_j}\right] + P_k - \beta^* \rho\omega k \tag{7}$$

$$\frac{\partial \rho U_j \omega}{\partial x_j} = \frac{\partial}{\partial x_j}\left[\left(\mu + \sigma_\omega \mu_t\right)\frac{\partial \omega}{\partial x_j}\right] + P_\omega - \beta\rho\omega^2 + 2(1 - f_1)\frac{\rho\sigma_{\omega 2}}{\omega}\frac{\partial k}{\partial x_j}\frac{\partial \omega}{\partial x_j} \tag{8}$$

Let k represent the turbulent kinetic energy, ω represent the turbulent dissipation rate, P_k and P_ω represent the production terms for the terms k and ω respectively, while μ_t represents the turbulent viscosity.

P_k and P_ω can be expressed as follows

$$P_k = \mu_t \Omega^2 \text{ and } P_\omega = C_\omega \rho \Omega^2 \tag{9}$$

Ω denotes the vorticity magnitude. The turbulent viscosity μ_t is defined as follows:

$$\mu_t = \frac{a_1 k}{max\left(a_1\omega, f_2 \|\Omega\|\right)} \tag{10}$$

Where: a_1 represents the experimental constant with a value of 0.31, k is the turbulent kinetic energy, ω stands for the specific dissipation rate, and f_2 is the blending function, characterized by the equation (11):

$$f_2 = tanh\left(\Gamma_2^4\right) \tag{11}$$

The calculation of the blending equation (f_1) is performed using the following expression:

$$f_1 = tanh\left(\Gamma_1^4\right) \tag{12}$$

The effectiveness of diffusivity, Γ_2 *and* Γ_1, can be expressed through equations (13) and (14) as follows:

$$\Gamma_2 = max\left(\frac{2\sqrt{k}}{0.09\omega d}, \frac{500\mu}{\omega d^2}\right) \tag{13}$$

$$\Gamma_1 = min\left[max\left(\frac{\sqrt{k}}{0.09\omega d}, \frac{500\mu}{\omega d^2}\right), \frac{4\rho\sigma_{\omega 2} k}{CD_{K\omega} d^2}\right] \tag{14}$$

Where: d is the distance to the nearest wall and $CD_{k\omega}$ represents the positive portion of the cross-diffusion term, which is derived from the equation given by Eq. (15).

$$CD_{k\omega} = \max\left(2\rho\sigma_{\omega 2}\frac{1}{\omega}\frac{\partial k}{\partial x_j}\frac{\partial \omega}{\partial x_i}, 10^{-20}\right) \tag{15}$$

The constants ϕ in the new model are determined through the following calculation based on the constants ϕ_1 and ϕ_2:

$$\phi = f_1 \phi_1 + (1 - f_1)\phi_2 \tag{16}$$

The constants are as follows [46]:

$$\kappa = 0.41,\ a_1 = 0.31,\ \sigma_{k1} = 0.85,\ \sigma_{k2} = 1.0,\ \sigma_{\omega 1} = 0.5$$

$$\sigma_{\omega 2} = 0.856,\ \beta_1 = 0.075,\ \beta^* = 0.09,\ C_{\omega 1} = 0.533,\ C_{\omega 2} = 0.44$$

The Nusselt number can be determined using the equation (17) [49]:

$$Nu = \frac{h\, q}{\lambda (T_w - T_b)} \tag{17}$$

Here, T_w and T_b denote the local temperature of the heated cube and the local bulk temperature of the fluid, respectively, while q represents the heat flux.

Mesh implementation

The convergence of simulations is significantly affected by the execution of the grid. In order to achieve prompt and precise simulation convergence, considerable care should be devoted to the process of generating the grid [50]. The simulations conducted utilized a structured hexahedral grid, which was generated via the use of ANSYS ICEM. Figure 4a depicts the mesh structure in the proximity of the electronic component within the designated domain. Figure 4b portrays the mesh situated in close proximity to

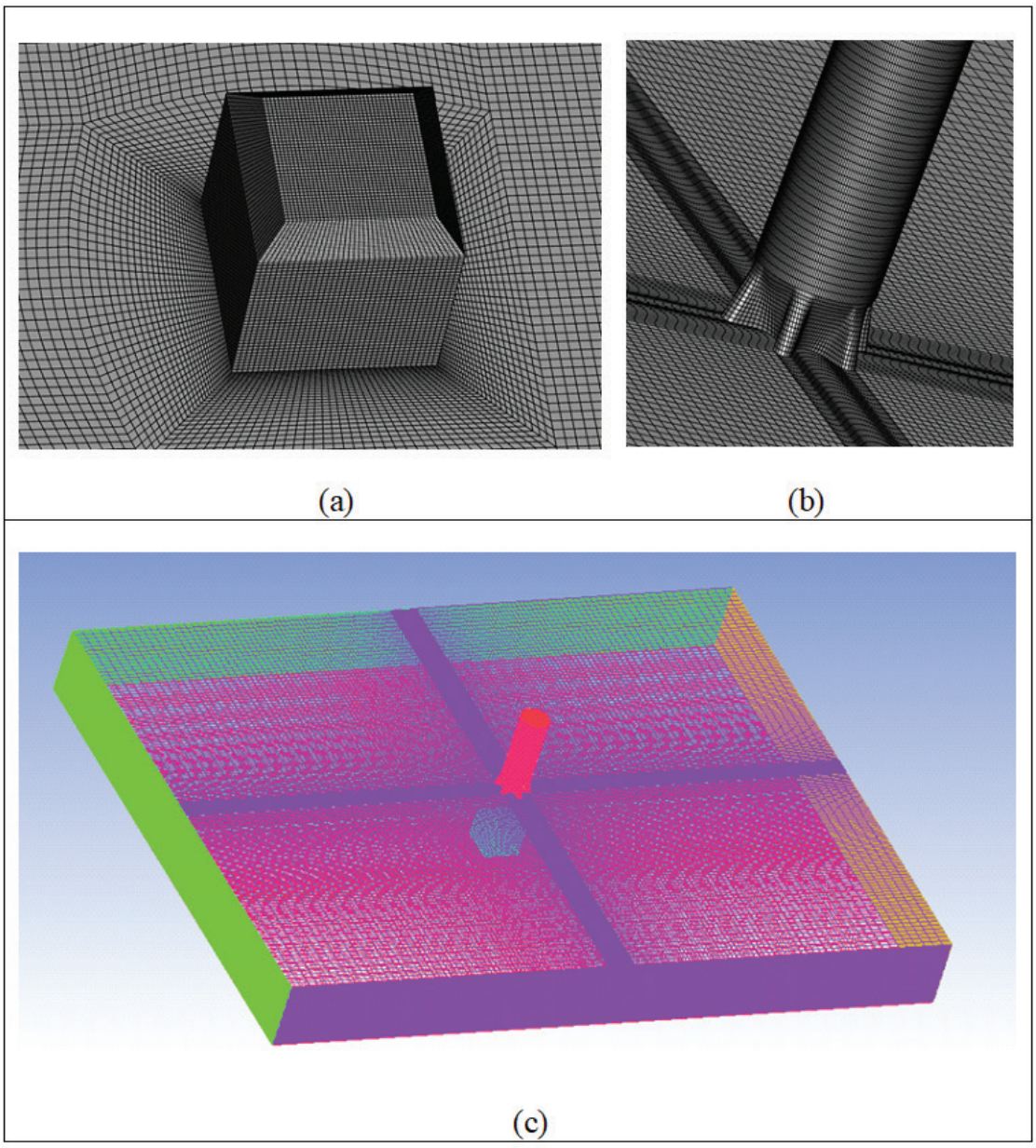

Figure 4. (a) Mesh adjacent to the cube, (b) Mesh in proximity to the diffuser, (c) Computational grid.

Table 2. Properties of the various meshes for the selected configuration

Grid	Cell size	Y+	Nusselt number
Grid 1	1514014	3.708	29.76
Grid 2	2129400	1.500	29.86
Grid 3	4526300	0.218	28.59
Grid 4	5410068	0.215	28.52

the diffusers. Figure 4c illustrates the procedure of mesh generation in the computational domain.

For this study, it was crucial to tackle the equations of continuity, energy, momentum, and turbulence. To carry out this task, the Ansys Fluent software [51] and SIMPLEC algorithm were employed. In order to generate precise results, a three-dimensional persistent simulation was initiated. The simulation focused on three cube shapes, comprising of a regular, chamfered, and rounded cube. The *k-ω* a turbulence model for reliable shear stress was used. Ensuring numerical stability was of utmost importance, and hence, a second-order central differential was adopted to calculate the diffusive term of the transport equation. Moreover, a second-order updraft scheme was applied to handle the adjective term. Using the PRESTO technique, we came up with the nominal values for typographic terminology.

In order to strike a balance between accuracy and computational resources, we employed four different grid sizes to evaluate the solution's reliance on grid quality and cell dimensions. The regular cube served as the fundamental structure for our simulations. The specifications and characteristics of these grids, all featuring a hexahedral configuration, are presented in Table 2. Within this context, the equation $y^+ = u_t y/v$ played a vital role in the simulations [52], where y represents the distance measured perpendicular to the nearest wall, u denotes the friction velocity, and v signifies the kinematic viscosity of the fluid [4].

By fine-tuning near the boundaries, we successfully achieved a maximum value of 0.2 for the *y*+ parameter on the front, side, and rear surfaces, while the top surface exhibited a *y*+ value of 0.6, as illustrated in Figures 5 and 6. For this specific study encompassing all three cube geometries, Grid 3 was employed, comprising a total of 4526300 nodes.

Figure 7 shows the dimensionless velocity profiles for the calculated numerical results and the experimental data at the selected axial location. Overall, it can be seen that the calculated transverse flow velocity profiles are in good agreement with the experimental data at almost all locations.

The orthogonal quality metric, resulting from the analysis, is calibrated within a range spanning from zero to one. Values approaching zero signify a decrease in quality, in contrast to values nearing one, which indicate an enhancement in quality [52]. Illustrated in Figure 8, it is evident that the orthogonal quality above the cube indicates a value of 0.6 or higher. Moreover, the residual section of the computational domain exhibits an enhancement in quality which approaches a one.

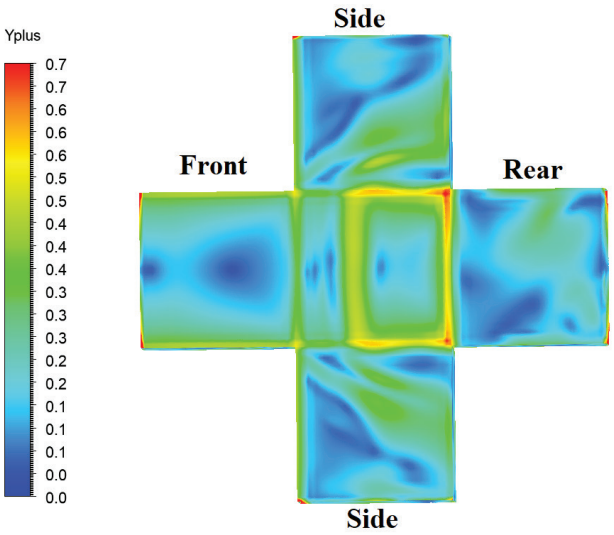

Figure 5. Evaluation of y+ values on the surfaces of the electronic component.

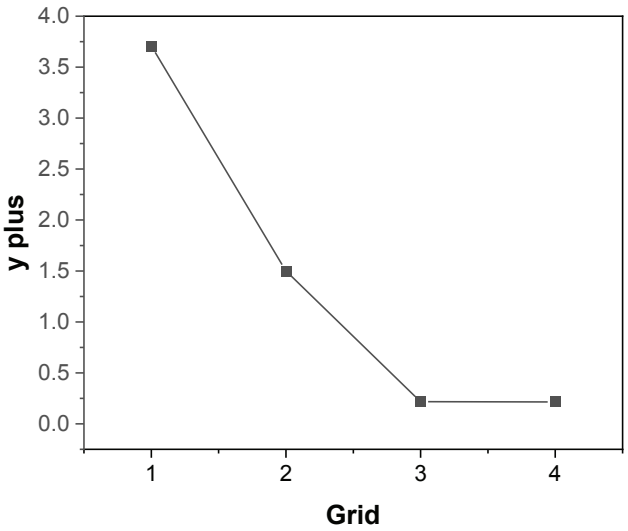

Figure 6. Variation of y+ with different meshes.

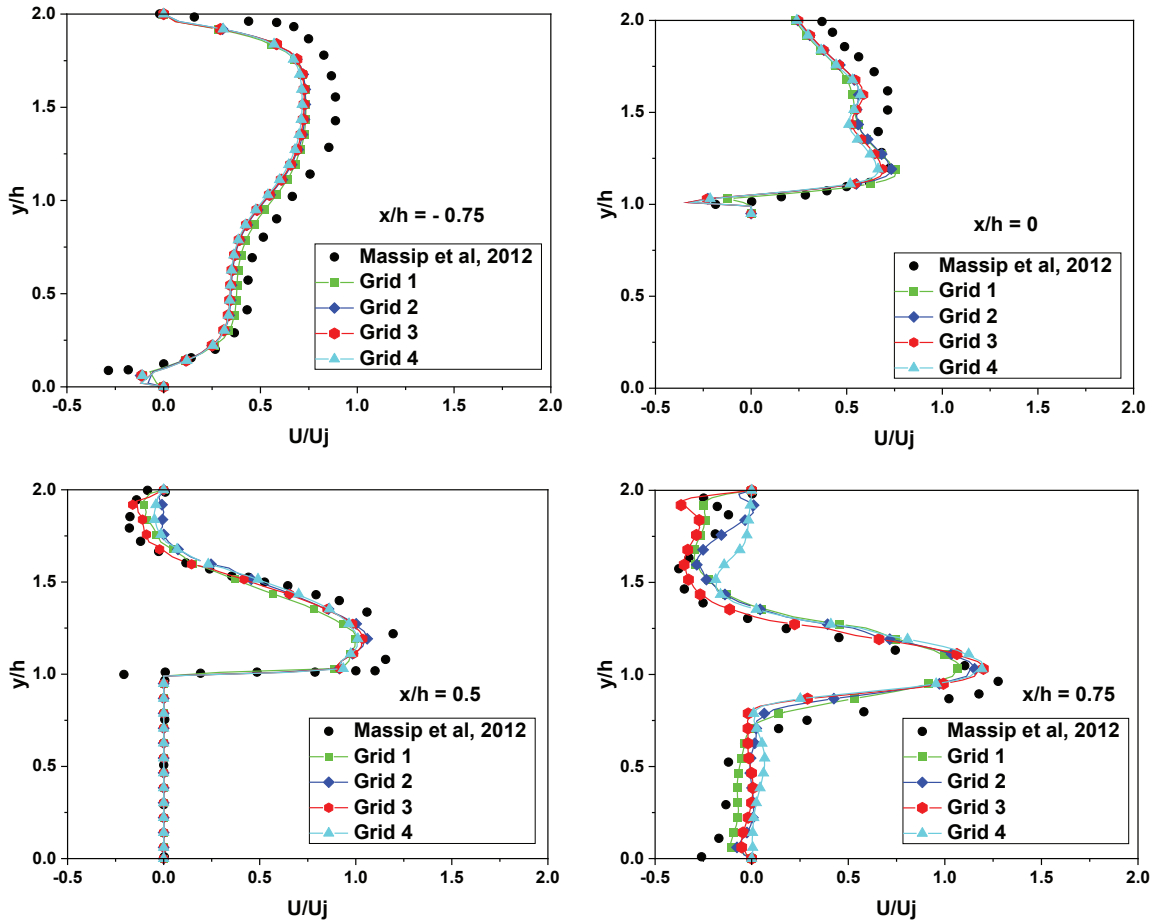

Figure 7. Comparison of transverse velocity profiles at selected axial locations and z=0 for different mesh sizes with experimental data.

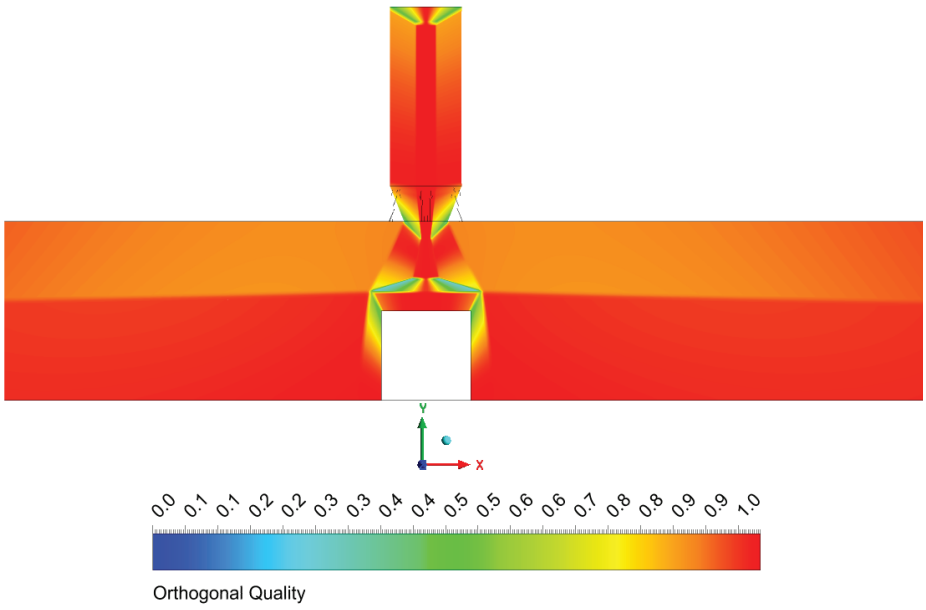

Figure 8. Orthogonal quality for the domain at z=0.

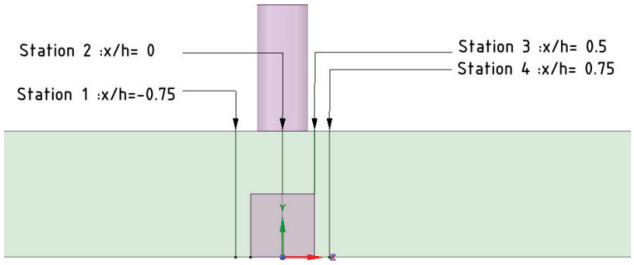

Figure 9. Illustrates the locations of stations where comparisons with experimental data are conducted.

Figure 9 presents a quantitative analysis of longitudinal velocity recorded at distinct locations preceding and succeeding the cube. The *SST k-ω* model appears to have successfully replicated the expected pattern with a high degree of accuracy.

RESULTS AND DISCUSSION

Figure 10 presents a visual display of the comparative analysis between our computational results and the corresponding experimental data in varying locations. The longitudinal speed profiles demonstrate significant agreement with the empirical ones at virtually all locations. Significant differences are discerned in particular portions of the profiles pertaining to station x/h = - 0. 75, which can be mainly attributed to variations in the inlet boundary conditions as well as the limitations of the turbulence modeling technique employed within the context of RANS methodology. Drawing upon the discovered results, it can be posited with confidence that the utilized model, grid, and parameters have successfully undergone the process of validation.

Figure 11 illustrates the contours of streamlines at z = 0, through the use of velocity magnitude colour mapping. This study elucidates the emergence of various fluid flow patterns which are contingent upon the specific geometry of the cube and the magnitude ratio of Reynolds number (Re_j/Re_H).

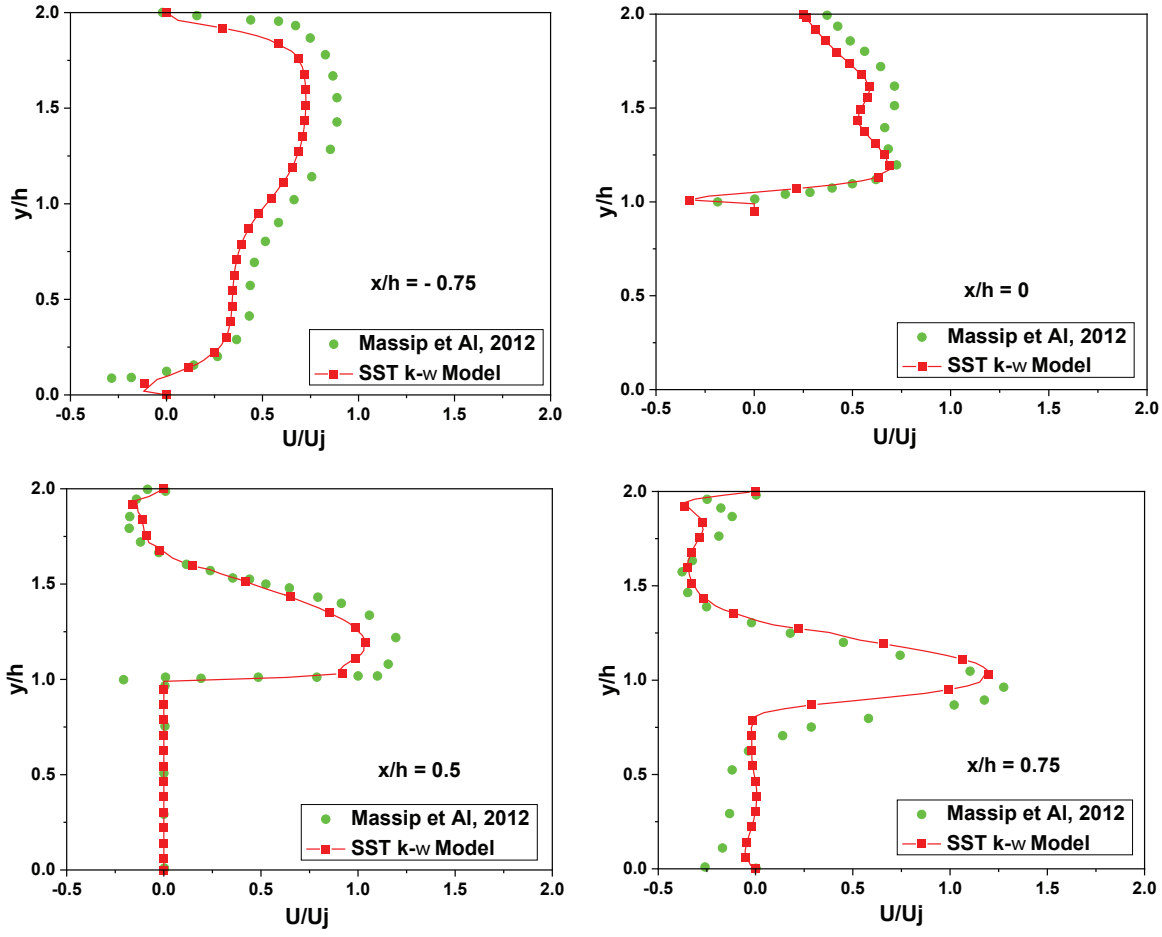

Figure 10. Comparison between streamwise dimensionless velocity profiles (U/Uj) and experimental data at specific axial positions, with z=0.

With α = Re_j/Re_H set to 0.5, flow separation results in the formation of a bound vortex atop the cube. However, the presence of chamfered and rounded edges reduces the size of this vortex. A distant upper vortex (labelled as 1 in reference [22]) emerges due to the interaction between the incoming flow and the jet flow. This upper vortex is absent when chamfered and rounded cubes are utilized. Similarly, a lower vortex (referred to as the Lower Horseshoe Vortex, denoted by 3 in reference [22]) is generated in the lower part of all cubes. It originates from the interaction between the cross flow and the lower section of the front face, positioned near the lower wall of the channel and upstream from the front face. For α = Re_j/Re_H equal to 1, The emergence of a recirculation zone in the wake region as a result of flow separation behind the component is one of the flow features. This zone re-joins the bottom wall downstream of the back face. For all cube situations, the size of this constrained vortex grows. At α = 1.5, the identical vortices witnessed in preceding scenarios manifest with increased dimensions in the current observations. Additionally, the utilization of rounded edges and chamfered surfaces leads to a greater sweep of jet flow across both the rear and front faces. This phenomenon enhances cooling efficiency, particularly noticeable in the case of the rounded cube.

The local Nusselt number distributions on the cube face, when unfolded and projected onto a plane, are depicted in Figure 12. It is evident that increasing the impinging to cross-flow ratio results in a clear rise in the Nusselt number for all cube geometries. For α = 0.5, the Nusselt number contours appear similar in the chamfered and rounded cube geometries. However, there is a noticeable improvement in cooling efficiency on the upper face of the regular cube. The front and upper faces of the cube exhibit high Nusselt number values, indicating effective heat transfer. However, caution is needed as there are localized hot spots on the lateral and rear faces, which could lead to thermal stresses and damage to electronic components. At α = 1, the cooling performance improves, particularly on the upper, lateral, and rear faces of the cube for all three geometries. The chamfered and rounded cubes show a significant increase in heat flux on the top face, with the chamfered cube benefiting more from the Upper Horseshoe Vortex developed on this surface. For α = 1.5, the Nusselt number levels surpass those at α = 0.5 and 1.0, indicating improved

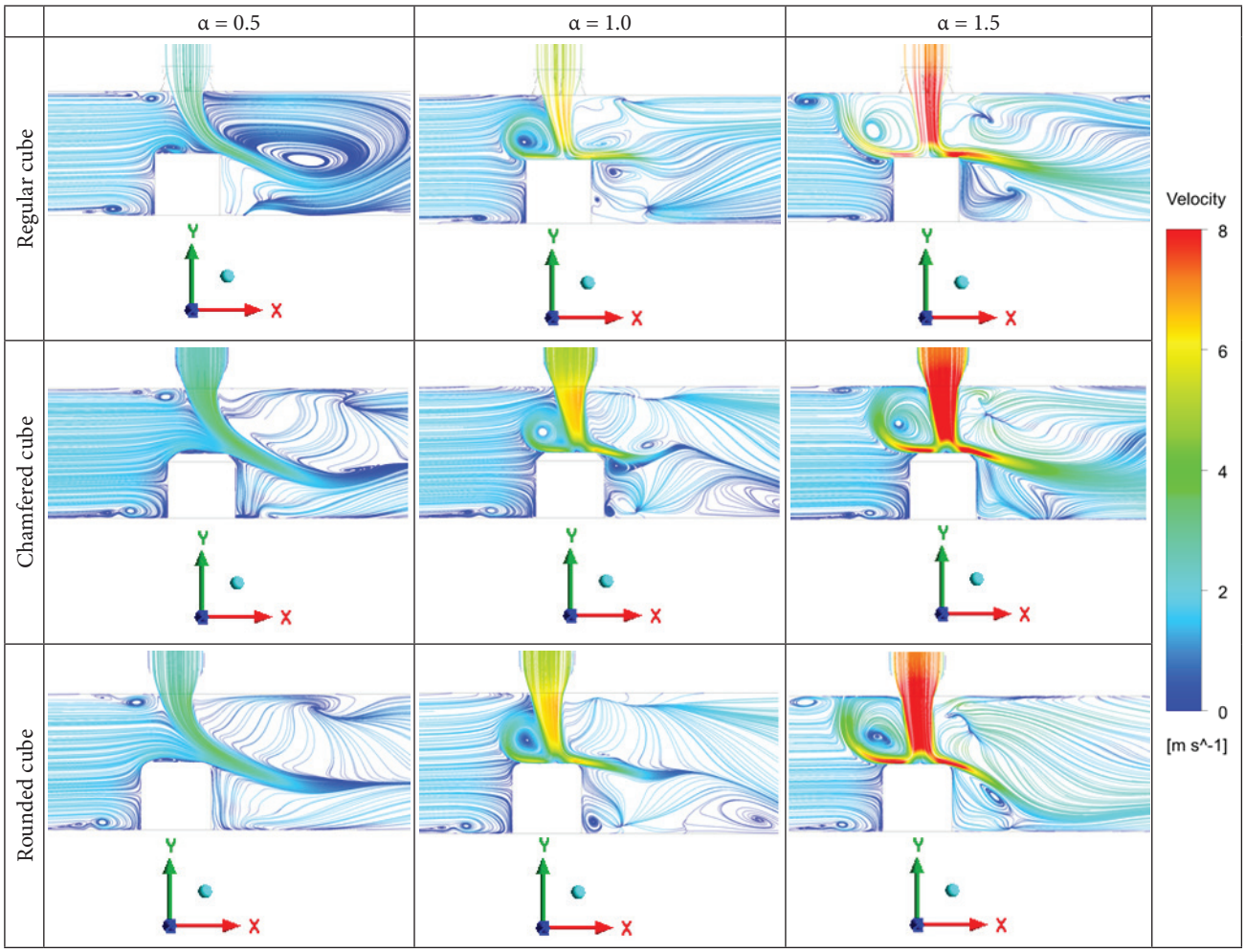

Figure 11. Streamlines visualized using velocity magnitude color mapping at z/h=0.

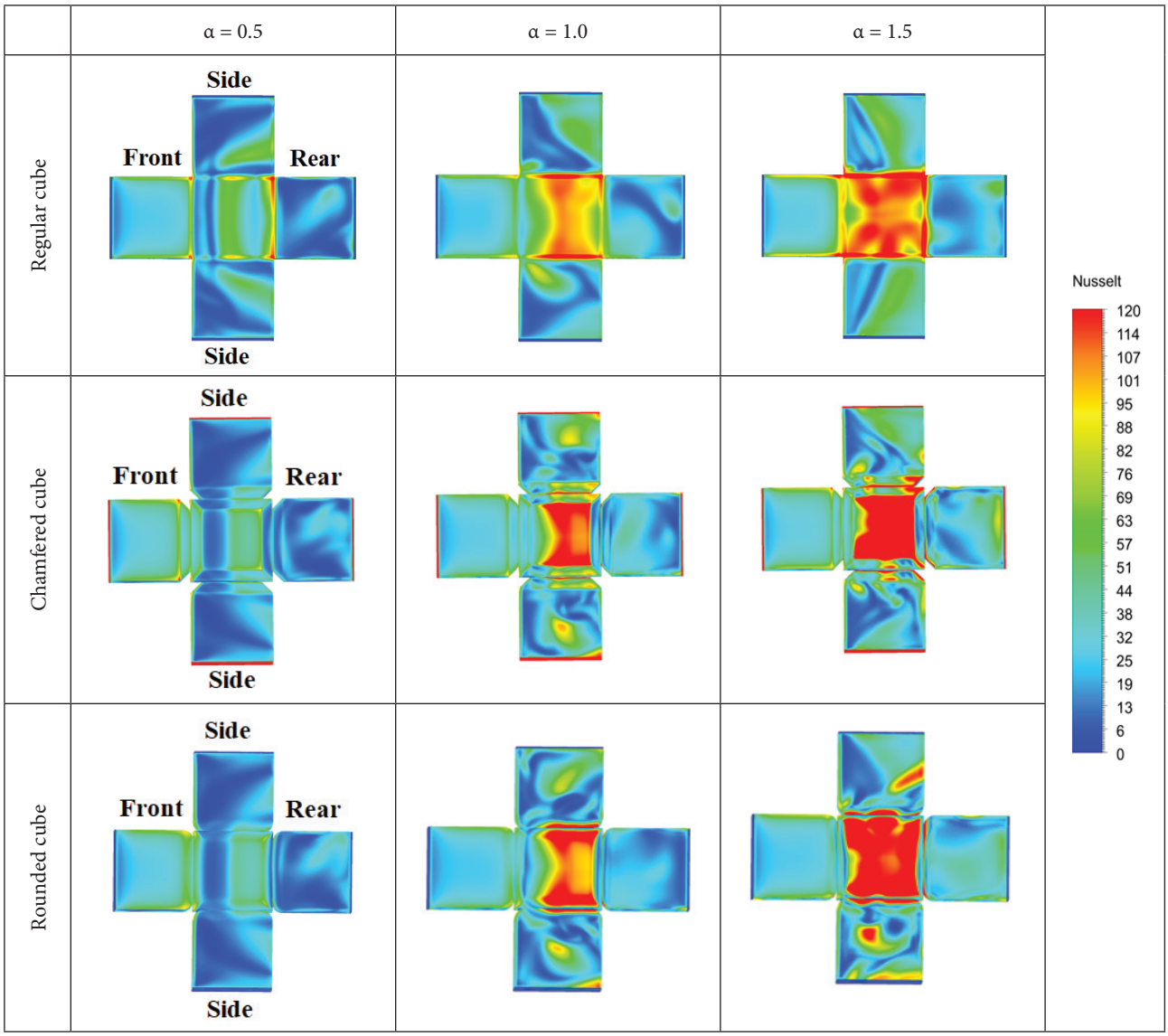

Figure 12. Demonstrates contour plots that illustrate the local Nusselt number on the surfaces of the electronic component in different cube geometries.

heat transfer across all cube faces. The upper face experiences the most significant enhancement when transitioning from a circular to lobed diffuser geometry. Furthermore, the rounded and chamfered edges contribute to increased heat flux, with the rounded cube demonstrating a more pronounced effect, resulting in enhanced cooling of electronic components. From these findings, it can be concluded that the lobed jet improves cooling efficiency for all Reynolds number ratios. Additionally, there is a direct relationship between flow morphology (diffuser type and electronic component geometry) and heat flux efficiency.

Figure 13 exhibits the tridimensional vertical architectural arrangement of nine instances, depicted utilizing the iso-surface of the Q-criterion and chromatically differentiated by velocity magnitude. At the value of α = 0.5, the coherent structures demonstrate a remarkable resemblance among the three configurations of the cube. The interplay between the transverse velocity field and the fluid emanating radially from the jet precipitates the formation of a discernible, superior horseshoe vortex (UHV). Moreover, the magnitude of the ultra-high vacuum (UHV) enlarges in tandem with the escalation of the Reynolds number ratio. A lower horseshoe vortex emerges adjacent to the lower wall of the channel due to the interaction between the transverse flow and the front surface of the block, and further extends in the downstream direction on both sides. The findings indicate that the chamfered and rounded cube shapes exhibit comparable LHV dimensions that outperform those of the regular cube, thereby facilitating optimal cooling. Furthermore, when α = 1.5, significant interference is

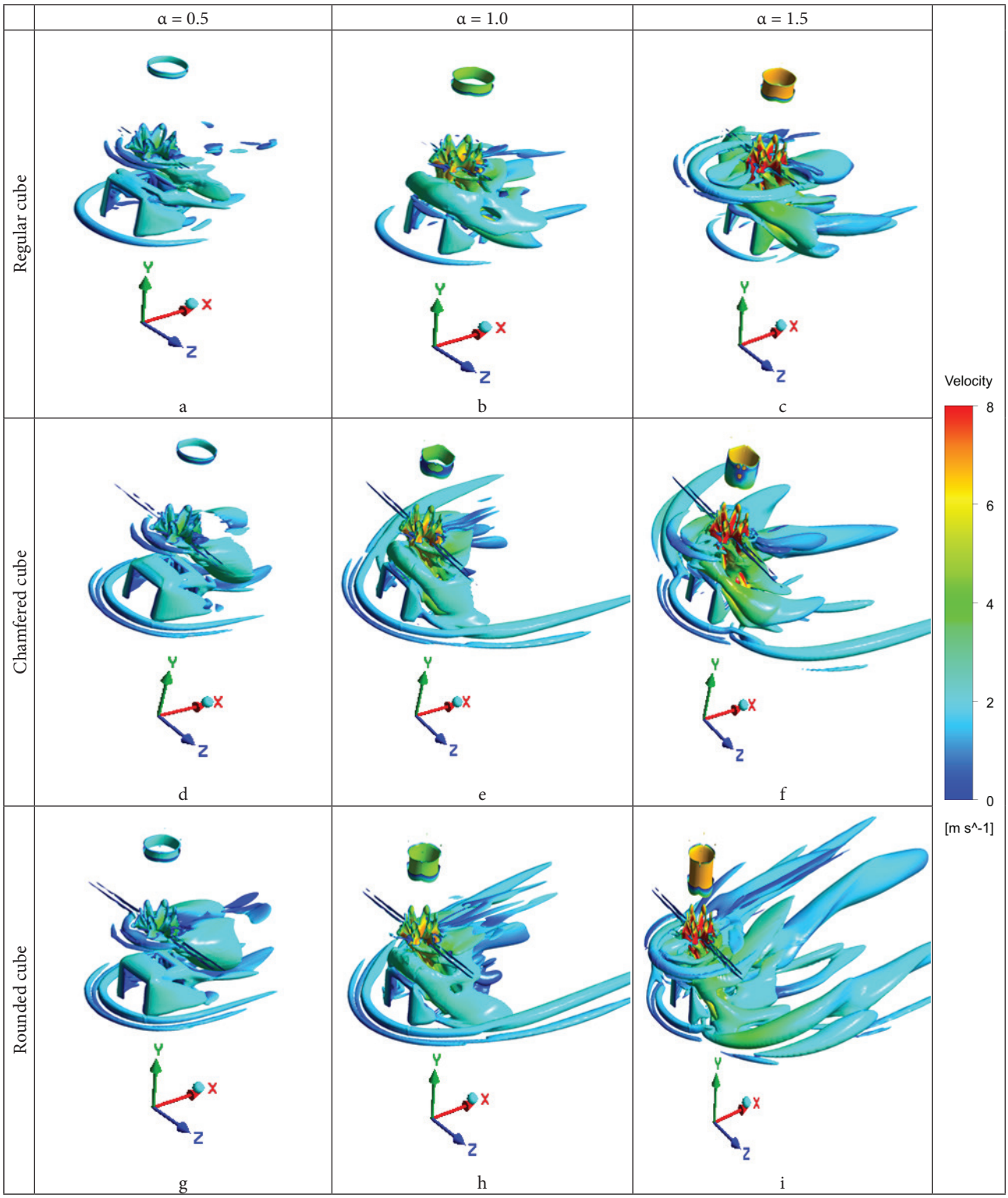

Figure 13. Three-dimensional vertical formations represented by the iso-surface of Q-criterion ($Q=10^{-2}\ s^{-2}$), with the colouring indicating the magnitude of the velocity.

observed between the upper horseshoe vortex and lower horseshoe vortex (LHV).

Figure 14 shows the relationship between the average Nusselt number and the Reynolds number ratio (α). The results reveal a positive correlation between the ratios of average Nusselt number and Reynolds number in various cube configurations, indicating improved heat transfer with increasing Reynolds number. Each configuration studied represent

Table 3. Correlation analysis of average Nusselt number to Reynolds number ratios across different cube configurations

Configurations	Correlation coefficients	Nu correlations
Regular cube	0.99918974	Nu =21.5 α+19
Chamfered cube	0.980608572	Nu =26 α+14
Rounded cube	0.999260081	Nu =30 α+9.3333333

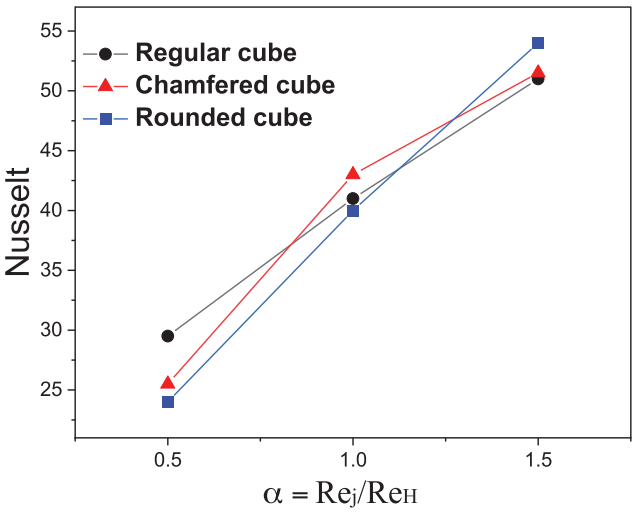

Figure 14. Exhibits the average Nusselt number corresponding to varying Reynolds number ratios.

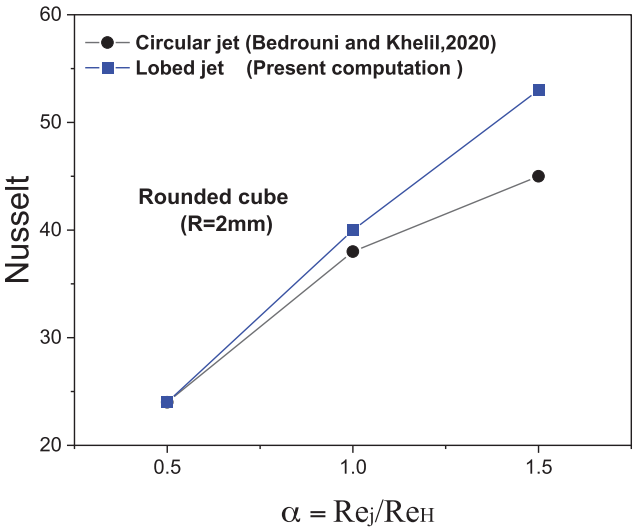

Figure 15. Comparison between the lobed jet investigated in the current study and the circular jet studied by Bedrouni and Khelil [3]. The average Nusselt number as a function of Reynolds number ratios.

perfect, positive correlations and the correlation coefficients that approach the value 1. Presented in Table 3 as follows:

It seems that the correlation between the average Nusselt number and the ratio of Reynolds number (α) is positive, which seems to be the correct relationship. As the ratio of the Reynolds number (α) increases, the average Nusselt number increases, which means that they tend to move in the same direction of each other, and it can be seen from the above result that the relationship is linear. This result is very significant in the case of the rounded cube configuration (Table 3). Several Nusselt number correlation according to the Reynolds number ratio (α) are presented in Table 3. There is a strong significant relationship between the average Nusselt number and the Reynolds number ratio α, because the slope is very strong for the configuration of the rounded cube (Table 3). At α = 0.5, cubes with rounded edges and chamfered corners show a decrease in cooling efficiency. However, of the examined cube configurations, the regular cube (referred to as cube 1) demonstrates superior cooling efficiency, with a Nusselt number of 29. For α = 1.0, only the chamfered cube exhibits improved cooling efficiency, reaching average Nusselt number of 43, an increase of 4.7% compared to cube 1. With α=1.5, the rounded cube has the highest cooling performance, with a Nusselt number of 53, exceeding the ordinary cube by more than 3.7%.

A comparison between the lobed jet used in the present study and the circular jet resulting from the numerical investigation carried out by Bedrouni and Khelil [3] is presented in Figure 15. The analysis focuses on a cube with rounded edges of R = 2 mm, examining the average Nusselt number as a function of ratios of Reynolds numbers. For α = 0.5, the average Nusselt number remains similar for circular and lobed jets, indicating comparable heat transfer performance. When α = 1.0, the lobed jet patterns demonstrate a slight improvement in heat flux over the circular jet, with an average Nusselt number of 40, representing a 5% improvement over the circular jet. However, for α = 1.5, the lobed diffuser shows superior cooling performance, exhibiting a Nusselt number of 53. This value is more than 15% higher than that of the circular jet, indicating a significant improvement in efficiency. Heat transfer for the lobed configuration compared to the circular configuration.

CONCLUSION

This study investigated the effects resulting from alterations in jet diffuser geometry and subtle adjustments to the upper cube face, encompassing features such as rounded edges and chamfered corners, on the efficacy of cooling electronic components. There are multitudes of cooling

techniques available for electronic components, encompassing finned heat sink, confined jet impingement, geothermal energy and heat pipes. The implementation of various cooling methods, such as airflows, liquid-cooled dielectric systems, Nano fluids, thermoelectric effects and liquid immersion systems. All these new methods have improved the thermal performance of electronic equipment.

Several Nusselt number correlation according to the Reynolds number ratio (α) are presented. There is a strong significant relationship between the average Nusselt number and the Reynolds number ratio α, because the slope is very strong for the configuration of the rounded cube.

Across all cube geometries, an increase in the impinging to cross-flow Reynolds number ratio resulted in improved heat flux. However, at α = 0.5, cubes with rounded edges and chamfered corners exhibited lower cooling efficiency compared to regular cubes. Thus, it is recommended to prioritize the use of regular cubes to enhance cooling effectiveness in this scenario.

At α = 1.0, the cooling efficiency was enhanced exclusively in the case of the chamfered cube, surpassing other cube designs with an average Nusselt number showing a 4.7% increase compared to the regular cube. Additionally, the lobed jet configurations demonstrated a slight improvement in heat flux compared to the circular jet, with an average Nusselt number reflecting a 5% enhancement.

Furthermore, at α = 1.5, the rounded cube displayed superior cooling performance, surpassing the regular cube by over 3.7% based on the Nusselt number. Notably, the lobed diffuser exhibited outstanding cooling effectiveness, with a Nusselt number of 53, surpassing the circular jet by over 15%. This significant improvement highlights the efficacy of the lobed configuration in enhancing heat transfer efficiency.

In conclusion, these findings provide valuable insights into the effects of diffuser geometry modifications and cube configurations on cooling effectiveness for electronic components. They enable informed decisions in optimizing cooling strategies, offering potential improvements in electronic component cooling.

NOMENCLATURE

D	Nozzle jet diameter *(m)*
H	Channel height *(m)*
h	Cube height *(m)*
k	Turbulent kinetic energy, $(m^2\ s^{-2})$
Nu	Nusselt number
p	Pressure, *Pa*
P_k, P_ω	Production terms of k and ω respectively
Pr_t	Turbulent Prandtl number
q	Heat flux *(W)*
Re_H	Cross flow Reynolds number based in the cube height and the inlet velocity
Re_j	Impinging jet flow Reynolds number based in the nozzle diameter and the jet velocity
S	Strain rate tensor, (s^{-1})
$\|\|S\|\|$	Norm of strain rate tensor
T	Temperature *(K)*
U_H	Cross flow velocity inlet, (ms^{-1})
U_J	Jet velocity inlet, (ms^{-1})
x, y, z	Cartesian coordinate system, *(m)*
y^+	Wall units coordinate, *(–)*

Greek symbols

δ_{ij}	Kronecker tensor, *(–)*
ε	Dissipation of turbulent kinetic energy $(m^2\ s^{-3})$
Ω	Antisymmetric vortex tensor
ω	Turbulent dissipation rate
μ	Dynamic viscosity $(m^2\ s^{-1})$
μ_t	Turbulent viscosity $(m^2\ s^{-1})$
ρ	Density, $(kg\ m^{-3})$
λ	Thermal conductivity $(W\ m^{-1}\ K^{-1})$
$\alpha = Re_j/Re_H$	Impinging to cross flow Reynolds number ratio

Subscripts

i, j, k	Coordinate alternation indices
t	Turbulent
$(..)'$	Fluctuating quantity
$(..)^+$	Dimensionless quantity

Abbreviations

CFD	Computational fluid dynamic
LES	Large eddy simulation
LHV	Lower horseshoe vortex
PIV	Particle Image Velocimetry
RANS	Reynolds Averaged Navier Stokes
RSM	Reynolds Stress Model
SST	Shear stress transport
SV	Side vortex
UHV	Upper horseshoe vortex
WV	Wake vortex

AUTHORSHIP CONTRIBUTIONS

Authors equally contributed to this work.

DATA AVAILABILITY STATEMENT

The authors confirm that the data that supports the findings of this study are available within the article. Raw data that support the finding of this study are available from the corresponding author, upon reasonable request.

CONFLICT OF INTEREST

The author declared no potential conflicts of interest with respect to the research, authorship, and/or publication of this article.

ETHICS

There are no ethical issues with the publication of this manuscript.

FUNDING

This work was carried out by the DGRSDT.

REFERENCES

[1] Meslem A, Bode F, Nastase I, Martin O. Optimization of lobed perforated panel diffuser: Numerical study of orifice geometry. Mod Appl Sci 2012;6:59−73. [CrossRef]

[2] Khelil A, Naji H, Loukarfi L, Meliani MH, Braikia M. Numerical simulation of the interactions among multiple turbulent swirling jets mounted in unbalanced positions. Appl Math Model 2016;40:3749−3763. [CrossRef]

[3] Bedrouni M, Khelil A. Numerical study on the performance of rounded corners on the top of electronic components on cooling effectiveness. Int J Heat Mass Transf 2020;150:119391. [CrossRef]

[4] Braikia M, Naji H, Khelil A, Maammar A. Experimental and CFD-based study of the interaction of lobed multi-jet diffusers in unbalanced positions. J Braz Soc Mech Sci Engineer 2022;44:264. [CrossRef]

[5] Ingole S. Temperature analysis for the horizontal target cooling with non-confined and inclined air jet. J Ther Engineer 2023;9:342−355. [CrossRef]

[6] Popovac M, Hanjalić K. Large-eddy simulations of flow over a jet-impinged wall-mounted cube in a cross stream. Int J Heat Fluid Flow 2007;28:1360−1378. [CrossRef]

[7] Kanbur BB, Wu C, Fan S, Duan F. System-level experimental investigations of the direct immersion cooling data center units with thermodynamic and thermoeconomic. Energy 2020;217:119373. [CrossRef]

[8] Hussain CM. Handbook of Nanomaterials for Industrial Applications: Micro and Nano Technologies. Amsterdam: Elsevier; 2018.

[9] Datta A, Halder P. Field-synergy and nanoparticle's diameter analysis on circular jet impingement using three oxide-water-based nanofluids. J Therm Engineer 2023;9:179-190. [CrossRef]

[10] Jalili B, Jalili P. Numerical analysis of airflow turbulence intensity effect on liquid jet trajectory and breakup in two-phase cross flow. Alexandria Engineer J 2023;68:577−585. [CrossRef]

[11] Jalili P, Ganji DD, Nourazar SS. Investigation of convective-conductive heat transfer in geothermal system. Results Phys 2018;10:568−587. [CrossRef]

[12] Jalili P, Kazerani K, Jalili B, Ganji DD. Investigation of thermal analysis and pressure drop in non-continuous helical baffle with different helix angles and hybrid nano-particles. Case Stud Ther Engineer 2022;36:102209. [CrossRef]

[13] Kaplan S, Bayramoğlu K, Sarikanat M, Altay L. Numerical study on heat transfer and fluid dynamics in plate heat exchangers: Effects of chevron angle and aspect ratio. J Therm Engineer 2024;10:638−656. [CrossRef]

[14] Jalili B, Aghaee N, Jalili P, Domiri Ganji D. Novel usage of the curved rectangular fin on the heat transfer of a double-pipe heat exchanger with a nanofluid. Case Stud Therm Engineer 2022;35:102086. [CrossRef]

[15] Rupesh PL, Raja K, Sathyaseelan, Sunil Kumar K, Vijaydharan S, Mohan Reddy AM, et al. Experimental evaluation of thermal stress on the surface of butterfly specimen through irreversible colour change of thermal paint. Mater Today Proc 2022;59:1768−1775. [CrossRef]

[16] Kumar KS, Muniamuthu S, Mohan A, Amirthalingam P, Muthuraja MA. Effect of charging and discharging process of PCM with paraffin and Al2O3 additive subjected to three point temperature locations. J Ecol Engineer 2022;23:34−42. [CrossRef]

[17] Kumar KS, Raju BN, Arulmani J, Amirthalingam P. Design and structural analysis of liquified cryogenic tank under seismic and operating loading. Int J Mech Engineer Technol 2016;7:345−366.

[18] Castro IP, Robins AG. The flow around a surface-mounted cube in uniform and turbulent streams. J Fluid Mech 1977;79:307−335. [CrossRef]

[19] Hearst RJ, Gomit G, Ganapathisubramani B. Effect of turbulence on the wake of a wall-mounted cube. J Fluid Mech 2016;804:513−530. [CrossRef]

[20] Tummers MJ, Flikweert MA, Hanjalić K, Rodink R, Moshfegh B. Impinging jet cooling of wall mounted cubes. In: Procedings of the ERCOFTAC International Symposium on Engineering Turbulence Modelling and Measurements; 2005 May 23-25; Sardinia, Italy; 2005. pp. 773−782. [CrossRef]

[21] Nakamura H, Igarashi T, Tsutsui T. Local heat transfer around a wall-mounted cube. Int J Heat Mass Transf 2001;44:3385−3395. [CrossRef]

[22] Masip Y, Rivas A, Larraona GS, Anton R, Ramos JC, Moshfegh B. Experimental study of the turbulent flow around a single wall-mounted cube exposed to a cross-flow and an impinging jet. Int J Heat Fluid Flow 2012;38:50−71. [CrossRef]

[23] Attalla M, Abdel Samee AA, Salem NN. Experimental investigation of heat transfer of impinging jet on a roughened plate by a micro cubic shape. Exp Heat Transf 2020;33:210−225. [CrossRef]

[24] Saleha N, Fadèla N, Abbès A. Improving cooling effectiveness by use of chamfers on the top of electronic components. Microelectron Reliab 2015;55:1067−1076. [CrossRef]

[25] Boudraa B, Bessaïh R. Three-dimensional turbulent forced convection around a hot cubic block exposed to a cross-flow and an impinging jet. Heat Transf 2021;50:413−431. [CrossRef]

[26] Macia YM, Rodriguez Soto AA, Nunez Gonzalez SM, Yanes JP. Parametric study of electronic cooling by means of a combination of crossflow and an impinging jet. IEEE Access 2022;10:103749−103764. [CrossRef]

[27] Khan BA, Saha AK. Turbulent flow and heat transfer characteristics of an impinging jet over a heated wall-mounted cube placed in a cross-flow. Phys Fluids 2022;34:025120. [CrossRef]
[28] Joshi T, Parkash O, Krishan G. Estimation of energy consumption and transportation characteristics for slurry flow through a horizontal straight pipe using computational fluid dynamics. Phys Fluids 2023;35:053303. [CrossRef]
[29] Joshi T, Parkash O, Krishan G. CFD modeling for slurry flow through a horizontal pipe bend at different Prandtl number. Int J Hydrogen Energy 2022;47:23731−23750. [CrossRef]
[30] Joshi T, Parkash O, Krishan G. Slurry flow characteristics through a horizontal pipeline at different Prandtl number. Powder Technol 2023;413:118008. [CrossRef]
[31] Joshi T, Parkash O, Krishan G, Murthy AA. Numerical investigation of Bi-model slurry transportation through horizontal pipe bend. Powder Technol 2023;418:118284. [CrossRef]
[32] Meslem A, Nastase I, Allard F. Passive mixing control for innovative air diffusion terminal devices for buildings. Build Environ 2010;45:2679−2688. [CrossRef]
[33] Meslem A, El Hassan M, Nastase I. Analysis of jet entrainment mechanism in the transitional regime by time-resolved PIV. J Vis 2011;14:41−52. [CrossRef]
[34] Choi SK, Kim SO. Turbulence modeling of natural convection in enclosures: A review. J Mech Sci Technol 2012;26:283−297. [CrossRef]
[35] Joshi T, Parkash O, Krishan G. Numerical investigation of slurry pressure drop at different pipe roughness in a straight pipe using CFD. Arab J Sci Engineer 2022;47:15391−15414. [CrossRef]
[36] Joshi T, Parkash O, Murthy AA, Krishan G. Numerical investigation of Bi-model slurry transportation in a straight pipe. Results Eng 2023;17:100858. [CrossRef]
[37] Koseoglu MF, Baskaya S. The effect of flow field and turbulence on heat transfer characteristics of confined circular and elliptic impinging jets. Int J Ther Sci 2008;47:1332−1346. [CrossRef]
[38] Podila K, Rao Y. CFD modelling of supercritical water flow and heat transfer in a 2 × 2 fuel rod bundle. Nucl Engineer Des 2016;301:279−289. [CrossRef]
[39] Zahout N, Braikia M, Khelil A, Naji H. Thermal and dynamic characterization of a multi-jet system with different geometry diffusers. J Therm Engineer 2024;10:404−429. [CrossRef]
[40] Prasad KSR, Krishna V, Bharadwaj S. Effect of heat flux and mass flux on the heat transfer characteristics of supercritical carbon dioxide for a vertically downward flow using computational fluid dynamics and artificial neural networks. J Therm Engineer 2023;9:1291−1306. [CrossRef]
[41] Attou Y, Bouhafs M, Feddal A. Numerical analysis of turbulent flow and heat transfer enhancement using V-shaped Grooves mounted on the Rotary Kiln's outer Walls. J Therm Engineer 2023;10:350-359. [CrossRef]
[42] Khelil A, Naji H, Braikia M, Loukarfi L. Comparative investigation on heated swirling jets using experimental and numerical computations. Heat Transf Engineer 2015;36:43−57. [CrossRef]
[43] Wasewar KL, Sarathi JV. CFD Modelling and simulation of jet mixed tanks. Engineer Appl Comput Fluid Mech 2008;2:155−171. [CrossRef]
[44] Wilcox DC. Reassessment of the scale-determining equation for advanced turbulence models. AIAA J 1988;26:1299−1310. [CrossRef]
[45] Basiri M, Goshayeshi HR, Chaer I, Pourpasha H, Heris SZ. Experimental study on heat transfer from rectangular fins in combined convection. J Ther Engineer 2023;9:1632−1642. [CrossRef]
[46] Menter FR. Review of the shear-stress transport turbulence model experience from an industrial perspective. Int J Comput Fluid Dyn 2009;23:305−316. [CrossRef]
[47] Safaei MR, Togun H, Vafai K, Kazi SN, Badarudin A. Investigation of heat transfer enhancement in a forward-facing contracting channel using FMWCNT nanofluids. Numer Heat Transf Appl 2014;66:1321−1340. [CrossRef]
[48] Nadooshan AA, Mohammadi S, Bayareh M. Heat transfer and friction characteristics of an array of perforated fins under laminar forced convection. J Ther Engineer 2019;5:115−122. [CrossRef]
[49] Rana S, Dura HB, Bhattrai S, Shrestha R. Impact of baffle on forced convection heat transfer of CuO/water nanofluid in a micro-scale backward facing step channel. J Ther Engineer 2022;8:310−322. [CrossRef]
[50] Kumar SK, Bishnoi D. Pressure exertion and heat dissipation analysis on uncoated and ceramic (Al2O3, TiO2 and ZrO2) coated braking pads. Mater Today Proc 2023;74:774−787. [CrossRef]
[51] ANSYS. ANSYS Fluent Theory Guide. Available at: https://dl.cfdexperts.net/cfd_resources/Ansys_Documentation/Fluent/Ansys_Fluent_Theory_Guide.pdf. Accessed Jun 26, 2024.
[52] Kilic M, Ullah A. Numerical investigation of effect of different parameter on heat transfer for a crossflow heat exchanger by using nanofluids. J Ther Engineer 2021;7:1980−1989. [CrossRef]